applied sciences

MDPI

Article

Mathematical Analysis and Real-Time Control of a Novel 5-DOF Robotic System with a Parallel Kinematics Structure for Additive Manufacturing Technologies

Ahmet Dumlu [1,*], Kagan Koray Ayten [1], Mehran Mahboubkhah [2], Gurkan Kalınay [1], Sadrettin Golcugezli [3] and Sina Akhbari [2]

1 Department of Electrical & Electronic Engineering, Erzurum Technical University, Erzurum 25550, Turkey; kagan.koray@erzurum.edu.tr (K.K.A.); gurkan.kalinay@erzurum.edu.tr (G.K.)
2 Department of Mechanical Engineering, University of Tabriz, Tabriz 5166616471, Iran; mahboobkhah@tabrizu.ac.ir (M.M.); s_akhbari@tabrizu.ac.ir (S.A.)
3 Department of Electrical & Electronic Engineering, Ataturk University, Erzurum 25550, Turkey; sadrettin.golcugezli@atauni.edu.tr
* Correspondence: ahmetdumlu@erzurum.edu.tr

Abstract: The systems that use parallel kinematic structures in additive manufacturing technology are particularly notable for their ability to provide exceptional precision and efficiency in the fabrication of intricate geometrically shaped items. This study introduces a novel system paradigm with five degrees of freedom, specifically developed to tackle existing additive manufacturing issues. In the proposed design, by incorporating rotational motions along the x and z axes, contributions were added to the efficiency of typical three-degrees-of-freedom (3-DOF) systems, resulting in a total of five degrees of freedom. In this way, it is aimed at increasing product durability, improving surface integrity, and saving production time. In this study, the conceptual design of the system was defined. Mathematical analyses were then used to determine the kinematic and dynamic models of the system, and a proposed model-based control technique was revealed. To evaluate the axis movement performance of the system, two different control techniques were used, and real-time test studies were conducted. The first control technique was the proportional–integral–derivative (PID) controller, and the second method was the sliding mode control (SMC) method, which was used to increase the performance of the system during trajectory tracking. The experimental results showed that the SMC method provides a reasonably good trajectory tracking response and a steady-state error compared to the classical PID controller.

Keywords: rapid prototyping; additive manufacturing; robotic manufacturing; prototype manufacturing; sliding mode control (SMC); PID control; 5-DOF 3D printer; dynamic; kinematic; robotic control

Citation: Dumlu, A.; Ayten, K.K.; Mahboubkhah, M.; Kalınay, G.; Golcugezli, S.; Akhbari, S. Mathematical Analysis and Real-Time Control of a Novel 5-DOF Robotic System with a Parallel Kinematics Structure for Additive Manufacturing Technologies. *Appl. Sci.* **2024**, *14*, 1482. https://doi.org/10.3390/app14041482

Received: 19 January 2024
Revised: 7 February 2024
Accepted: 9 February 2024
Published: 12 February 2024

1. Introduction

Additive manufacturing technology has brought about a profound shift in the manufacturing sector in recent years and is widely regarded as a fundamental pillar of the third industrial revolution. Additive manufacturing technology is an essential manufacturing strategy that responds to today's more complicated and personalized production demands. Additive manufacturing, in contrast to conventional manufacturing processes, employs a layer-by-layer approach to create products, thereby reducing material waste. This technique has a broad spectrum of applications, spanning from prototype manufacturing to the manufacture of intricate components. An important benefit of additive manufacturing is its ability to enhance design flexibility. The capacity to generate pieces of complexity that cannot be produced using conventional techniques provides designers and engineers with enormous freedom. This fosters creativity and expedites the process of developing new products. As per the article published in *The Economist* magazine in

April 2012, this technique has generated significant attention in both theory and application within the industry, particularly due to its ability to manufacture goods with intricate geometries [1,2]. Furthermore, the noteworthy aspect of smart additive manufacturing lies in its potential to be very customizable [3–6]. This approach, whereby each component may be independently manufactured, provides the chance to address client requirements promptly and efficiently. This attribute confers a competitive edge in the market when faced with the requirements of customized goods. Due to its benefits, such as the ability to adapt designs, quickly create prototypes, customize products, and save on materials, this technology has the capacity to enhance production procedures while simultaneously improving product quality and customer happiness. Hence, organizations are increasingly prioritizing the augmentation of their investments in additive manufacturing technology as a crucial strategy to uphold their competitive edge and promptly adapt to evolving market demands.

In traditional production methods using machine tools or printers with three linear degrees of freedom, additional add-ons called supports are used. These supports, while necessary, contribute to higher production costs and add complexity to the process. Recently, there has been a significant effort to advance additive manufacturing technology to address the constraints of traditional three-axis systems. Within these advancements, the creation of systems with diverse kinematic structures or more degrees of freedom has significant importance. Utilizing additive manufacturing technology, the utilization of robotic systems equipped with multi-axis parallel kinematic structures facilitates the production of complex-shaped components. These methods circumvent restrictions and enable items to be manufactured more effectively [7]. Within this framework, the improvement of additive manufacturing technology and the use of new kinematic structures could lead to better and more competitive solutions in business settings. This can be achieved by enhancing crucial aspects, such as product durability, surface integrity, and production efficiency. Parallel kinematic mechanisms are preferred in design studies for additive manufacturing technologies because they have the potential to provide greater precision, stiffness, agility, and processing speed compared to Cartesian systems.

In the past two decades, four-degrees-of-freedom (4-DOF) parallel mechanisms have garnered significant attention due to their inherent advantages, such as a relatively large workspace, compact structural features, notable load-bearing capabilities, and relatively straightforward motion control [8,9]. Various parallel robots capable of Schöenflies motion, such as H4, I4, Par4, and C4 mechanisms for high-speed pick-and-place manipulations, have been developed [10–13]. Initially, the H4 machine, based on the Delta robot concept, a 3T-1R parallel kinematic machine (PKM), was proposed, and its position and velocity relationships were analyzed. It was demonstrated that the H4 principle could serve as the foundation for a complete family of machines [14,15]. Subsequently, scholars in the field have designed and studied various types of 4-DOF parallel manipulators. Rolland [16] designed two 4-DOF parallel mechanisms. Briot et al. [17] presented a partially decoupled, four-degrees-of-freedom 3T1R parallel manipulator with high load-carrying capacity. Yi Lu et al. [18] proposed an over-constrained RRPU + 2UPU parallel manipulator (PM) with three legs. Briot et al. [19] introduced a novel 4-DOF decoupled parallel manipulator with Schönflies motions [20] called the Pantopteron-4. Yang et al. [21] presented a hierarchical approach for the type-synthesis of limb structures of the PKMs, with 3T1R motion with a variable rotational axis. In machining processes, particularly milling, it is crucial that the tool remains perpendicular to the workpiece surface throughout the machining process to avoid errors and ensure high-quality machining. However, existing 4-DOF parallel mechanisms either have a rotational DOF around the vertical axis or two rotational DOFs suitable for pick-and-place and positioning tasks. Studies have shown that using parallel kinematic structures with different layouts may shorten the time it takes to produce parts by increasing the number of degrees of freedom to four, mostly through turning around the z-axis [22]. A further investigation included the creation of a delta-type parallel kinematic framework that had the capability to rotate along the x-axis. This advancement enhanced the system's maneuverability [23]. Another study presented a high-speed parallel robot that exhibited Schönflies motion. In this study, the robot had great potential for achieving efficient and rapid pick-and-place manipulation in packaging manufacturing lines. The robot was equipped with four identical appendages and a solitary platform. The robot's small shape and single-platform idea provided it with a strong potential for dynamic responsiveness. The movement properties of the proposed robot are examined using a line graph approach that relies on Grassmann line geometry. This approach also incorporates a generalized Blanding rule to facilitate the translation between line graphs representing movements and restrictions. Afterward, the inverse kinematics is calculated, and the problem of singularity in the robot is examined using both qualitative and quantitative methods [24]. A novel parallel robot, Heli4, with four degrees of freedom, was provided in [25]. It drew inspiration from Delta architecture but was specifically engineered to surpass its constraints by including an articulated traveling plate. Contrary to the majority of articulated traveling plates, Heli4's moving plate was very small in size. Another research study introduced a novel parallel mechanism with four degrees of freedom that was specifically designed for manipulating heavy objects in a wide operating area [26]. The four degrees of freedom consisted of three translational movements and one rotational movement around a specified axis. This kind of mechanism is uncommon; the majority of parallel mechanisms typically contain either three or six degrees of freedom. Another study presented a specialized parallel manipulator with four degrees of freedom, which was designed for the purpose of pick-and-place tasks. Its development was aimed at achieving very high velocities. This research demonstrated that its design was well-suited for handling rapid changes and fluctuations. It was a development of the Delta, H4, and I4 robot designs, including the strengths of these robots while addressing their limitations [27]. Another example is an adaptive slicing method that can create ideal slices for five-axis hybrid layered manufacturing, allowing for deposition without the need for support structures. In contrast to the existing adaptive slicing method, this methodology differs not only in the thickness of each layer but also in the direction in which the object is sliced. The laser-aided manufacturing process (LAMP), a five-axis system that integrates both material additives and removal processes, was created at the University of Missouri-Rolla and serves as an illustrative example. The multi-degree-of-freedom technology enables the LAMP to construct a component with little support structures [28]. A novel creation called the unmanned robotic delta weapon platform (URDWP) is provided in [29]. The URDWP is an automated, teleoperated unmanned weapon system that securely retains and controls the actions of weaponry. This innovation is primarily characterized by the use of a delta robot equipped with three or more parallel kinematic chains (axes). Combat vehicles and unmanned defense vehicles are already equipped with remotely triggered weapons that are operated by robotic remote weapon platforms. Another work focused on the examination of the kinematics and dynamics of a new linearly actuated 4-DOF parallel kinematic machine. This machine was capable of performing three translational motions and one rotating motion. To achieve this objective, the inverse kinematic relations for position, velocity, and acceleration were determined using the closed-loop vector theorem. Next, the dynamics of the mechanism were analyzed using Euler's approach. Subsequently, a simulated dynamic model of the system was created [30].

Considering the aforementioned limitations, this paper proposes and develops a novel kinematic system design with a parallel kinematic structure as part of a range of research initiatives aimed at tackling the present obstacles in additive manufacturing technology. In contrast to conventional systems that include only three linear degrees of freedom, this research achieved five degrees of freedom by including rotational motions on the x and z axes. This feature was designed to enhance product durability, enhance the quality of wavy surfaces, and save manufacturing time.

In line with the above, the primary contribution of this paper is a novel 5-DOF parallel kinematic mechanism (3T2R), which, unlike its predecessors, has a rotational DOF around the x and z axes. In addition to the new proposed design, sliding mode control is performed for the first time in the literature on a multi-axis proposed system with five degrees of freedom for high-accuracy trajectory tracking control. In order to show the advantages of sliding mode control over the other classical control techniques, the classical PID method was applied to the proposed system as a second control approach. The design, implementation, and evaluation of a classical PID method and sliding mode control techniques for the motion control of a novel multi-axis system with five degrees of freedom are provided as the secondary contributions of this paper. The concept design of the proposed system, which includes mechanical components, is first presented, and then the kinematic and dynamic model of the system is determined via mathematical analysis. Then, the position analysis of the proposed system is realized. In order to determine the real-time performance of both controllers, experimental studies were conducted. Experimentally, it was validated that sliding mode control is an efficient and robust control method for the proposed system motion, including unmodeled dynamics. According to the experimental results, it was observed that the mathematical modeling for the proposed system was correct; the SMC method increased the trajectory tracking performance compared to the classical PID method during motion, and SMC is a more robust controller against the uncertainties of the system. The main contribution of this study to the literature is to offer a new perspective on production technologies, directing transformation in the industry, shaping future manufacturing processes, and triggering industrial innovation. The proposed system is presented in the literature as a production model that is more flexible, sustainable, cost-effective, precise, and capable of achieving high work speeds compared to traditional additive manufacturing methods.

The organization of the rest of the paper can be summarized as follows: The designed system structure, the kinematic and dynamic analysis of the 3D printer are presented in Section 2. Section 3 describes both the classical PID controller and nonlinear sliding mode control strategies. Section 4 presents the experimental findings, and Section 5 provides concluding remarks.

2. Design and Modelling of a 3D Printer with five Degrees of Freedom

The 3D printer system, seen in Figures 1 and 2, comprises a stationary platform and a movable platform that are interconnected with four kinematic chains. This platform consists of two PR (Pa)U and two PR (Pa)R kinematic chains. In the system, the terms R, P, U, and Pa correspond to rotary, prismatic, universal joint, and parallelograms, respectively. The fundamental element of kinematic chains is the planar, four-bar parallelogram structure. The parallelogram construction utilizes four separate linear rail systems to provide accurate control. The carriages, which form the parallelogram structure, are joined to each link via ball joints. The second and third arms are attached to the moving platform with ball joints, whereas the first and fourth arms have an indirect connection to the moving platform. Each connecting part is connected to the moving platform using a rotary joint. The present manipulator's moving platform has a construction that enables three degrees of freedom for translational movement and one DOF for rotating movement in the x-direction. This is shown in Figures 1 and 2. Utilizing a turntable enables the provision of rotating motion along the z-axis.

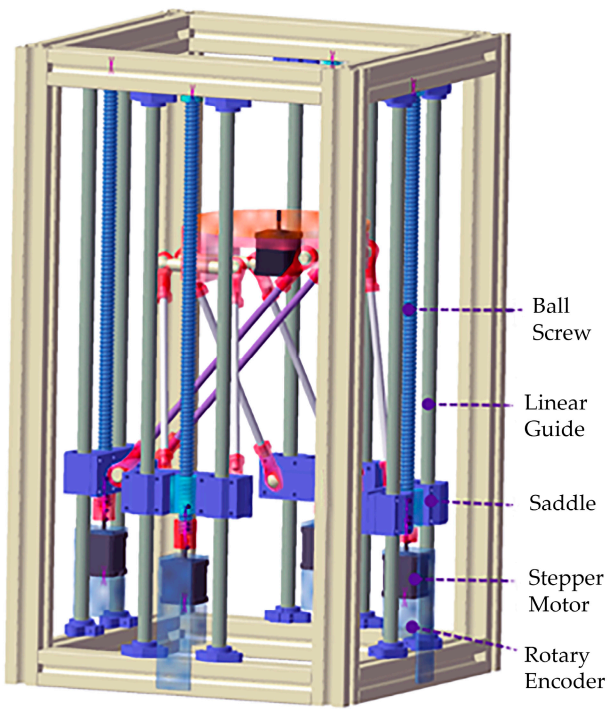

Figure 1. Structure of the proposed 5-DOF parallel mechanism.

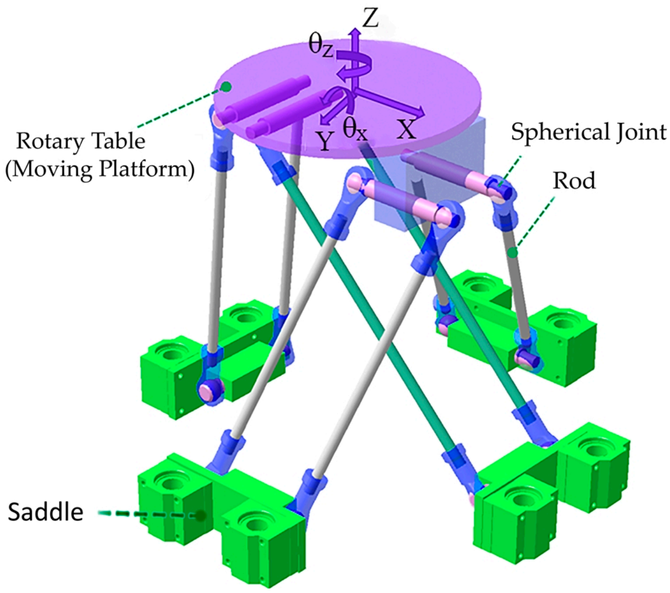

Figure 2. Connections and moving platform of the proposed 5-DOF parallel mechanism.

2.1. Inverse Kinematics of the Proposed 5-DOF 3D Printer Machine

Kinematic analysis refers to the process of determining the angular locations of the ties needed for a moving platform to achieve a certain position and orientation when the initial position and orientation values are specified. Precise kinematic analysis is essential for accurate system control and for efficiently determining the dynamic model of the system. Multiple approaches exist in the literature for the kinematic analysis of parallel processes. The methodologies included in this study are the Denavit-Hartenberg method, the geometric approach, the vector algebra method, and the Bezout method [31–34]. Furthermore, in recent years, researchers have used Nelder-Mead and genetic algorithms for the purpose of kinematic analysis [35,36]. The research used the vector algebra approach to conduct an inverse kinematic analysis of the mechanism. Figure 3 displays a vector representation of the system, which is used for the study. The index 'i' denotes a single kinematic chain out of several chains that are identical to each other. Figure 3 shows that the global coordinate system has an origin denoted as {O}, and it is determined by the x_o, y_o, and z_o components.

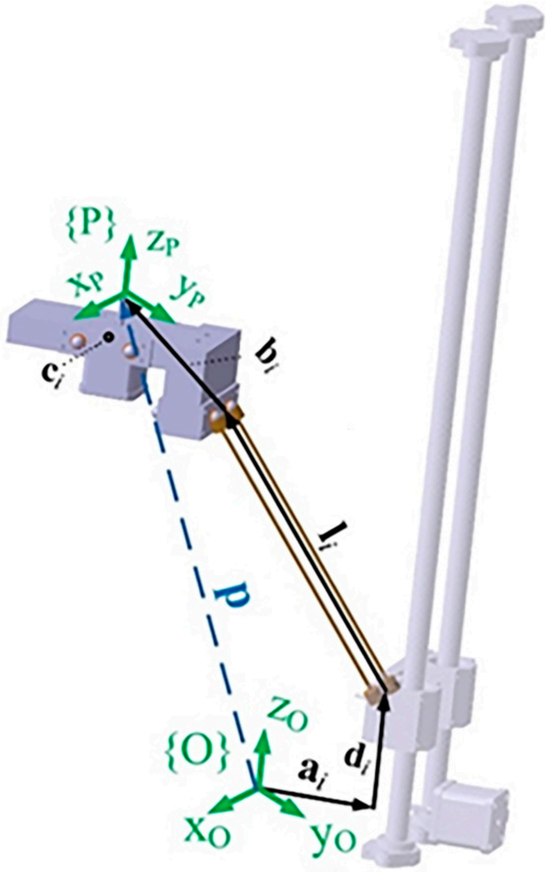

Figure 3. Vector notation for the kinematic modeling of the proposed manipulator.

For each prismatic joint, the vector a_i is used, connecting the origin of the global coordinate system and the beginning of the rail. The local starting point of the rail is the vector d_i, which is connected to the prismatic joint, i, on the car. The magnitude of the l_i vector seen in the figure is equal to the length of the ith connecting arm. Additionally, the vector c_i is a vector connected to the ith connector, starting from the midpoint of the spherical joints and ending at the rotary axis of the connector. However, for cases i = 2.4, the vector c_i is equal to 0 due to the structure of the mechanism. The vector b_i is fixed at the centre of the moving platform {P}, as indicated in Figure 3. At the same time, the vector b_i expresses the position of the parallelograms determined by the local frame. All the kinematic relationships are defined considering the fixed platform attached to the global frame {O}. Based on Figure 3, the vector equation for the ith kinematic chain can be expressed as Equation (1).

$$^{O}p + {}^{O}R_P{}^{P}b_i = {}^{O}a_i + {}^{O}d_i + {}^{O}l_i + {}^{O}c_i, \tag{1}$$

The vector must be defined according to the global coordinate system using the transformation formula provided in the following equation:

$$^{O}b_i = {}^{O}R_P{}^{P}b_i, \tag{2}$$

The expression denoted as ${}^{O}R_{P}$ in Equation (2) is a rotation matrix that is only defined in the x-direction, as shown in Equation (3), owing to the specific attributes of the mechanical system.

$$ {}^{O}R_{P} = R_x(\theta) = \begin{bmatrix} 1 & 0 & 0 \\ 0 & cos\theta_x & -sin\theta_x \\ 0 & sin\theta_x & cos\theta_x \end{bmatrix}, \tag{3} $$

In Equation (1), the vectors ${}^{O}d_i$ and ${}^{O}c_i$ are consistently aligned in the same direction. Due to this rationale, given that $\hat{d}_i$ represents the unit vector of vector d_i, Equation (1) may be restated as Equation (4) as follows:

$$ \left(p + b_i - a_i - c_i\hat{d}_i\right) - L_i = d_i\hat{d}_i, \tag{4} $$

In Equation (4), c_i and d_i denote the magnitudes of the vectors c_i and d_i, respectively. The vector expression L_i is represented as l_i and its value is provided. Equation (4) defines a sphere with a centre $p + b_i - a_i - c_i\hat{d}_i$ and radius l_i on the left side and a line running from the origin along $\hat{d}_i$ on the right side. Hence, the resolution of Equation (4) entails the point of convergence between a line and a well-defined sphere in a three-dimensional space. By using the above equivalences, the equation for d_i, may be derived as shown in Equation (5).

$$ d_i = -c_i + \hat{d}_i^T(p + b_i - a_i) \pm \sqrt{l_i^2 - (p + b_i - a_i)^T\left(I_{3\times3} - \hat{d}_i\hat{d}_i^T\right)(p + b_i - a_i)}, \tag{5} $$

Equation (5), obtained through vector analysis, characterises the scenario in which the mechanism is situated at a certain position and orientation. Using this equation, one may determine the necessary length d_i for the mechanism to achieve the specified position and orientation values.

2.2. Velocity and Acceleration Kinematics

To obtain the velocity vector $\dot{p}$ of the mobile platform of the mechanism, Equation (4) has to be differentiated with regard to time.

$$ \dot{p} + \dot{\theta}\hat{\imath} \times b_i = \dot{d}_i\hat{d}_i + \omega_{li} \times l_i, \tag{6} $$

The variable $\dot{\theta}$, represents the amplitude of the angular velocity of the moving platform in this equation. Performing the scalar multiplication of Equation (6) with the l_i vector yields Equation (7).

$$ \dot{d}_i = \frac{l_i}{\hat{d}_i.l_i}.\dot{p} + \frac{(\hat{\imath} \times b_i).l_i}{\hat{d}_i.l_i}\dot{\theta}, \tag{7} $$

Equation (7) was used to derive the matrix representation of the velocity kinematics of a mobile platform, transitioning from an angular format to a linear one. Equation (8) illustrates the outcome.

$$ \begin{bmatrix} \dot{d}_1 \\ \vdots \\ \dot{d}_4 \end{bmatrix} = \begin{bmatrix} \frac{l_1{}^T}{\hat{d}_1.l_1} & \frac{(b_1 \times l_1).\hat{\imath}}{\hat{d}_1.l_1} \\ \vdots & \vdots \\ \frac{l_4{}^T}{\hat{d}_4.l_4} & \frac{(b_4 \times l_4).\hat{\imath}}{\hat{d}_4.l_4} \end{bmatrix} \begin{bmatrix} \dot{p} \\ \dot{\theta} \end{bmatrix} = J \begin{bmatrix} \dot{p} \\ \dot{\theta} \end{bmatrix}, \tag{8} $$

The symbol J, as defined in Equation (8), denotes the Jacobian matrix of the system. The acceleration expression of a moving platform was obtained by taking the derivative of the velocity expression in Equation (6).

$$ \ddot{p} + \ddot{\theta}\hat{\imath} \times b_i + \dot{\theta}^2\hat{\imath} \times (\hat{\imath} \times b_i) = \ddot{d}_i\hat{d}_i + \dot{\omega}_{li} \times l_i + \omega_{li} \times (\omega_{li} \times l_i), \tag{9} $$

Performing the dot product of both sides of this equation with the vector l_i yields the formula for the acceleration of the prismatic joints in the system:

$$\dot{p} + \dot{\theta}\hat{i} \times b_i = \dot{d}_i\hat{d}_i + \omega_{li} \times l_i, \quad (10)$$

2.3. Dynamic Analysis

2.3.1. Inverse Dynamics

The primary objective of inverse dynamics analysis for any mechanism is to ascertain the requisite forces or torques at the end actuator of the mechanism in order to precisely track a certain trajectory. Essentially, these forces or torques are seen as a mathematical function that relies on the location, velocity, and acceleration of the system's joints, as well as the position of the mobile platform. The Euler technique was used in this work to deduce the analytical dynamic model of the specified system. The Euler approach stands out from other techniques, such as Lagrangian, due to its ability to address the computational time issue in real-time applications and provide a closed-form model in [37–41]. The Euler approach, applicable to any kinematic chain, treats each link as a rigid body. These connections may be individually examined and then merged. By using this method, the force or torque expressions that arise between the legs may be readily exposed. Consequently, this investigation included analysing the connections of each kinematic chain, beginning with the parallelogram and extending to the moving table, individually and sequentially.

Figure 4 displays a three-dimensional perspective of the mechanism and the geometric indices used in dynamic modelling. Given that the Euler technique was used to study each leg separately, it is necessary to assign each leg to its own local coordinate system. In order to address this issue, individual coordinate frames are denoted as $\{L_i\}$ being positioned inside each parallelogram structure. The connecting points of the connectors and parallelograms for each chain are represented by A_i, B_i, C_i, and D_i as illustrated in Figure 4. Furthermore, the E_i and D_i points denote the central points of the ball joints used for mounting the parallelogram onto the carriages utilized in the mechanism. On the other hand, the G_i and M_i points indicate the central points of the attachments utilized for connecting the parallelogram to the moving table in the mechanism.

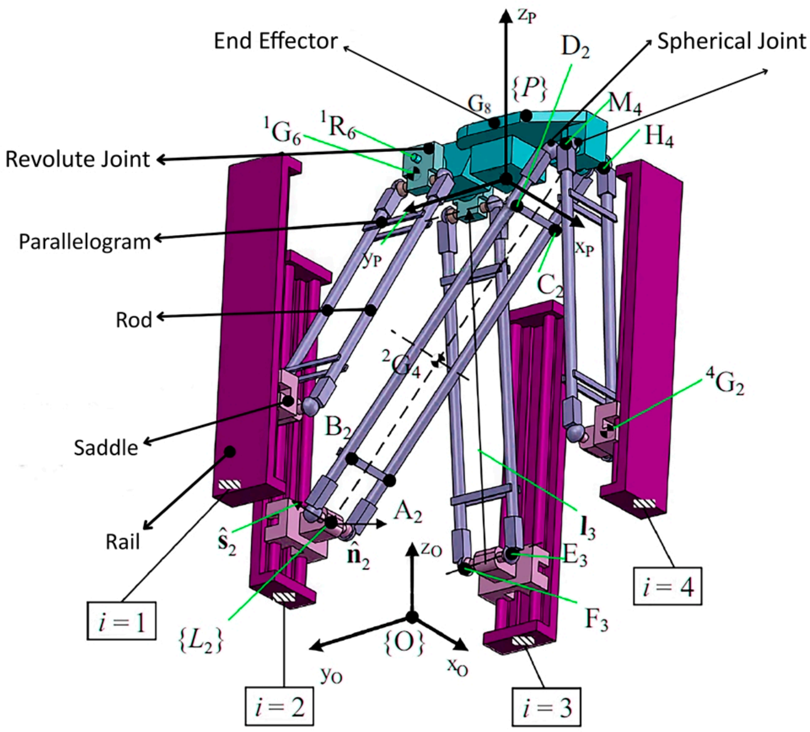

Figure 4. Freehand diagram of the mechanism.

Figure 4 displays the separate kinematic chains, with each component represented by circled integers ranging from one to eight. G_j^i denotes the centroid of each element, with the upper symbol i denoting the chain number and the lower sign j denoting the element number. Figure 5 displays the intricate free body diagram that is used in the dynamic analysis of the fully designed mechanism.

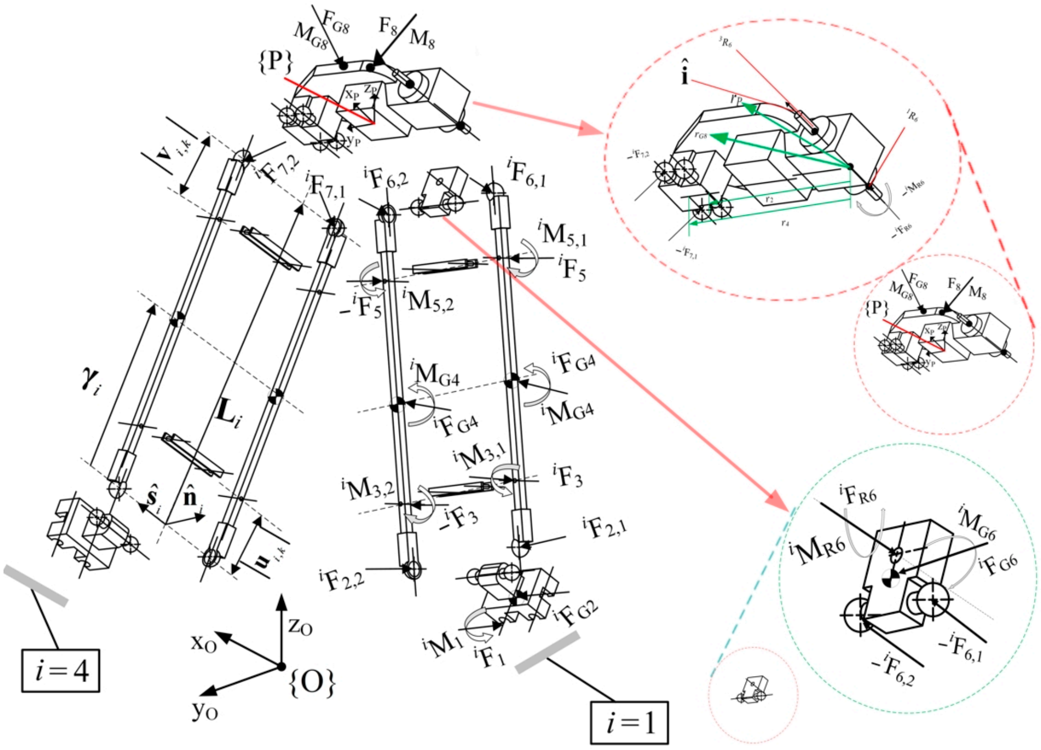

Figure 5. Detailed free-body diagram of the mechanism.

Given the similarity between the first and third kinematic chains, as well as the third and second kinematic chains, Figure 5 only provides detailed information on the first and fourth kinematic chains, together with the forces and torques acting on them. The spherical joints, $^iF_{j,k}$ (j = 2, 6, 7) seen in Figure 5, indicate the resultant force exerted on each leg of the parallelogram. In this context, the superscript i denotes the quantity of kinematic chains, the subscript j denotes the quantity of components, and k denotes the quantity of the joints used for connection in the parallelogram's legs. The forces and torques applied to the parallelogram connections via the connectors employed in the mechanism are denoted as $^iF_{j,k}$, $^iM_{j,k}$ (j = 3, 5) respectively. The forces and torques applied to the center of mass of each connecting component are denoted as $^iF_{G_j}$, $^iM_{G_j}$, respectively. The terms $^iF_{R_j}$, $^iM_{R_j}$ (j = 6) represent the rotational forces and torques that occur in the joints. In addition, $u_{i,k}$, $v_{i,k}$, as seen in Figure 5, denote the vectors that extend towards the connecting points A_i, B_i, C_i, and D_i of the parallelograms. The symbol γ_i denotes the vector that spans from the spherical joints to the center of mass of each leg of the parallelogram. As commonly understood, all forces and torques may be determined based on the reference point of the overall coordinate system of the mechanism using the Euler equation, which is represented as $\sum M_o = I_o\alpha + \omega \times I_o\omega$. In order to do this, we began by considering the moment equilibrium of both connections (k = 1, 2) for each parallelogram around the points E_i and F_i. Subsequently, we established their corresponding expressions reflected along the $\hat{n}_i$ axis. The mathematical representation of this scenario is provided in Equations (11) and (12).

$$\begin{pmatrix} u_{i,1} \times^i F_3 + \gamma_i \times^i F_{G_4} + v_{i,1} \times^i F_5 \\ +L_i \times^i F_{6,1} +^i M_{G_4} \end{pmatrix} \cdot \hat{n}_i + \left({}^i M_{3,1} +^i M_{5,1}\right) \cdot \hat{n}_i = 0 \quad (11)$$

$$\begin{pmatrix} -u_{i,2} \times^i F_3 + \gamma_i \times^i F_{G_4} - v_{i,2} \times^i F_5 + L_i \times^i F_{6,2} \\ +M_{G_4} \end{pmatrix} \cdot \hat{n}_i + \left(iM_{3,2} +^i M_{5,2}\right) \cdot \hat{n}_i = 0 \quad (12)$$

The equations ${}^iF_{G_4}$ and ${}^iM_{G_4}$, which are presented in Equations (11) and (12), respectively, are defined as shown in Equations (13) and (14).

$${}^iF_{G_4} = m_i\left(g -^i a_l\right), \quad (13)$$

$${}^iM_{G_4} = -\{\omega_i \times (I_{o,i}\omega_i) + I_{o,i}\dot{\omega}_i\}, \quad (14)$$

Here, g is the gravitational acceleration and m_i is the mass of the leg of the parallelogram. $I_{o,i} = \left({}^O_{L_i}T_i\right)\left(I_{L_i}\right)\left({}^O_{L_i}T_i{}^T\right)$ is the inertia matrix. This matrix is expressed in the global reference frame of the parallelogram and the origin of the global frame. The expression $I_{L_i} = I_{G_i} + m_l\|L_i\|^2 diag(0,\ 1,\ 1)$ is the inertia matrix of the parallelogram with respect to the origin of the global reference coordinate system shown in Figure 3. ${}^O_{L_i}T_i = \begin{bmatrix} \frac{L_i}{\|L_i\|} & \hat{n}_i \times \frac{L_i}{\|L_i\|} & \hat{n}_i \end{bmatrix}$, $i = 1, \ldots, 4$ is the equation placed on the $\{L_i\}$ leg according to the global coordinate system. It represents the transformation matrix of the local coordinate system. Equations (1) and (2) are added mathematically, and at the same time, considering that the legs in the system are connected to the system with the help of rotary joints, in other words, considering the equation provided in ${}^iM_{3,k} \cdot \hat{n} =^i M_{5,k} \cdot \hat{n} = 0, k = 1, 2,$ Equation (15) is obtained via the following:

$$(L_i \times \hat{n}_i) \cdot \left({}^iF_{6,1} +^i F_{6,2}\right) = 2\left(\gamma_i \times^i F_{G_4} +^i M_{G_4}\right) \cdot \hat{n}_i, \quad (15)$$

Furthermore, by considering the balance of the moment components around E_i, F_i along the $\hat{s}_i$ axis of the local coordinate system associated with the parallelograms, we obtained Equation (16).

$$\left(L_i \times \left({}^iF_{6,1} +^i F_{6,2}\right)\right) \cdot \hat{s}_i + 2\left(\gamma_i \times^i F_{G_4} +^i M_{G_4}\right) \cdot \hat{s}_i = 0, \quad (16)$$

By using the vector identity $(a \times b) \cdot c = (c \times a) \cdot b$, Equation (16) may be rewritten as Equation (17).

$$(L_i \times \hat{s}_i) \cdot \left({}^iF_{6,1} +^i F_{6,2}\right) = 2\left(\gamma_i \times^i F_{G_4} +^i M_{G_4}\right) \cdot \hat{s}_i, \quad (17)$$

By substituting the formulas derived from Equations (15) and (17) into the corresponding arms of the parallelograms in each kinematic chain, we obtain the following systems of equations:

$$\begin{bmatrix} N \\ S \end{bmatrix}_{8\times 12} \begin{bmatrix} 1F_{6,1} +^1 F_{6,2} \\ \vdots \\ 4F_{6,1} +^4 F_{6,2} \end{bmatrix} = \begin{bmatrix} R_N \\ R_S \end{bmatrix}, \quad (18)$$

Equations (19)–(22) express N, S, R_N, and R_S, respectively.

$$N = \begin{bmatrix} (L_1 \times \hat{n}_1)^T & 0 & 0 \\ 0 & \ddots & 0 \\ 0 & 0 & (L_4 \times \hat{n}_4)^T \end{bmatrix}_{4\times 12}, \quad (19)$$

$$S = \begin{bmatrix} (L_1 \times \hat{s}_1) & 0 & 0 \\ 0 & \ddots & 0 \\ 0 & 0 & (L_4 \times \hat{s}_4) \end{bmatrix}_{4\times 12}, \quad (20)$$

$$R_N = 2\begin{bmatrix} \left(\gamma_1 \times^1 F_{G_4} +^1 M_{G_4}\right) \cdot \hat{n}_1 \\ \vdots \\ \left(\gamma_4 \times^4 F_{G_4} +^4 M_{G_4}\right) \cdot \hat{n}_4 \end{bmatrix}, \tag{21}$$

$$R_S = 2\begin{bmatrix} \left(\gamma_1 \times^1 F_{G_4} +^1 M_{G_4}\right) \cdot \hat{s}_1 \\ \vdots \\ \left(\gamma_4 \times^4 F_{G_4} +^4 M_{G_4}\right) \cdot \hat{s}_4 \end{bmatrix}, \tag{22}$$

To derive the dynamic model of the system, it is necessary to articulate the forces and moments exerted on the connections located on the top moving platform of the system, as seen in Figure 2. To achieve this objective, by referring to Figure 5, the cumulative forces exerted on the mobile platform can be mathematically represented using Equation (23).

$$^iF_{R_6} =^i F_{6,1} +^i F_{6,2} -^i F_{G_6} \quad ,i = 1,3, \tag{23}$$

In this context, the symbol $^iF_{R_6}$ denotes the forces exerted on the connection by the rotary joint, and can be mathematically represented by Equation (24).

$$^iF_{G_6} = m_6\left(g -^i a_{Con}\right) \quad ,i = 1,3, \tag{24}$$

Similarly, based on the free body diagram shown in Figure 2, the moment components along the axis passing through, $^1R_6$ and $^3R_6$, can be represented by the equilibrium equation provided in Equation (25).

$$\left(r_4 \times \left(^4F_{7,1} +^4 F_{7,2}\right)\right) \cdot \hat{i} + \left(r_2 \times \left(^2F_{7,1} +^2 F_{7,2}\right)\right) \cdot \hat{i} = \left(r_{G_8} \times F_{G_8}\right) \cdot \hat{i} + M_{G_8} \cdot \hat{i} + \left(r_P \times F_8\right) \cdot \hat{i} + M_8 \cdot \hat{i} -^1 M_{R_6} \cdot \hat{i} -^3 M_{R_6} \cdot \hat{i}, \tag{25}$$

Here, the symbol $^iM_{R_6}$ $,i = 1,3$ indicates the moments exerted on the moving platform by the rotary joint of the connections. The symbols F_8 and M_8 represent the external forces and moments that are exerted on the moving platform, respectively. The forces and moments are explicitly represented by Equations (26) and (28).

$$F_{G_8} = m_8(g - a_{CP}), \tag{26}$$

$$M_{G_8} = -\left\{\dot{\theta}^2\hat{i} \times \left(I_{G_8}\hat{i}\right) + \ddot{\theta}I_{G_8}\hat{i}\right\}, \tag{27}$$

Considering the fact that $^iM_{R_6}$ $,i = 1,3$ does not have any components along $\hat{i}$, in other words, considering the $^1M_{R_6} \cdot \hat{i} =^3 M_{R_6} \cdot \hat{i} = 0$, relationship, Equation (25) can be rewritten as follows:

$$\left(\hat{i} \times r_4\right) \cdot \left(^4F_{7,1} +^4 F_{7,2}\right) + \left(\hat{i} \times r_2\right) \cdot \left(^2F_{7,1} +^2 F_{7,2}\right) = \left(r_{G_8} \times F_{G_8} + M_{G_8} + r_P \times F_8 + M_8\right) \cdot \hat{i}, \tag{28}$$

Furthermore, the total forces exerted on the mobile platform can be precisely described as stated in Equation (29).

$$\left(^4F_{7,1} +^4 F_{7,2}\right) + \left(^2F_{7,1} +^2 F_{7,2}\right) +^1 F_{R_6} +^2 F_{R_6}4 = F_{G_8} + F_8, \tag{29}$$

By substituting the expression for $^iF_{R_6}$ $,i = 1,3$ from Equation (23) into Equation (26), Equation (30) can be derived.

$$\left(^1F_{6,1} +^1 F_{6,2}\right) + \left(^2F_{7,1} +^2 F_{7,2}\right) + \left(^3F_{6,1} +^3 F_{6,2}\right) + \left(^4F_{7,1} +^4 F_{7,2}\right) = {}^1F_{G_6} +^3 F_{G_6} + F_{G_8} + F_8, \tag{30}$$

By using Equations (18), (28), and (30), the concept of force equality can be expressed in the form of a matrix, as shown in Equation (31).

$$\begin{bmatrix} ^1F_{6,1} +^1 F_{6,2} \\ ^2F_{7,1} +^2 F_{7,2} \\ ^3F_{6,1} +^3 F_{6,2} \\ ^4F_{7,1} +^4 F_{7,2} \end{bmatrix} = \Gamma^{-1}\Psi = \begin{bmatrix} I_{3\times3} & I_{3\times3} & I_{3\times3} & I_{3\times3} \\ 0 & \left(\hat{\imath} \times r_2\right)^T & 0 & \left(\hat{\imath} \times r_4\right)^T \\ & N & & \\ & S & & \end{bmatrix}^{-1} \cdot \begin{bmatrix} ^1F_{G_6} +^3 F_{G_6} + F_{G_8} + F_9 \\ \left(r_{G_8} \times F_{G_8} + M_{G_8} + r_P \times F_8 + M_8\right) \cdot \hat{\imath} \\ R_N \\ R_S \end{bmatrix}, \quad (31)$$

By treating the carriages and parallelograms as a unified rigid body, the equation below represents the combined forces acting on them:

$$^iF_1 = -\left\{^iF_{G_2} + 2^iF_{G_4} + \left(iF_{j,1} +^i F_{j,1}\right)\right\}, \; j = 6 \; for \; i = 1,3 \; and \; j = 7 \; for \; = 2,4, \quad (32)$$

The equation represented by $^iF_1$ denotes the forces exerted on the car by the rails used in the mechanism. The force F_{G_2} mentioned in the equation is defined as follows:

$$^iF_{G_2} = m_2\left(g - \ddot{d}_i\hat{d}_i\right), \quad (33)$$

Here, m_2 is the mass of the car. In this case, the value of the $^iF_1$ force acting on the system and extending along the vector $\hat{d}_i$, that is, the force f_a, can be defined as follows:

$$^if_a =^i F_1 \cdot \hat{d}_i, \quad (34)$$

As a result of these studies, Equation (35), which is based on Equations (31), (32), and (34), shows the matrix form of the inverse dynamic model of the system. This equation can be defined in the standard form used in control theory, as in Equation (36).

$$\begin{bmatrix} ^1f_a \\ \vdots \\ ^4f_a \end{bmatrix} = \begin{bmatrix} \hat{d}_1^T & 0 & 0 \\ 0 & \ddots & 0 \\ 0 & 0 & \hat{d}_4^T \end{bmatrix} \left[\Gamma^{-1}\Psi + \begin{bmatrix} ^1F_{G_2} + 2\left(^1F_{G_4}\right) \\ \vdots \\ ^4F_{G_2} + 2\left(^4F_{G_4}\right) \end{bmatrix} \right], \quad (35)$$

$$\tau = M(q)\ddot{q} + C(q,\dot{q})\dot{q} + G(q), \quad (36)$$

2.3.2. Dynamic Modeling of Stepper Motors Used in a 3D Printer

To achieve a certain path with the intended five-axis 3D printer, the actuators in the system need to be accurately controlled to move at a specific velocity and angle. A total of five hybrid stepper motors were used in the system's construction. There is no precise theoretical electromechanical equivalent model available to mathematically analyze these motors. To unveil the dynamic model of these motors, the magnetic equivalent circuit model was used instead of the electromechanical equivalent circuit [42–44]. The electrical equations for the phases of a stepper motor can be expressed using the magnetic equivalent circuit model, as shown in Equations (37) and (38).

$$U_a = Ri_a + L\frac{d}{dt}i_a - K_m\omega sin(p\theta), \quad (37)$$

$$U_b = Ri_b + L\frac{d}{dt}i_b - K_m\omega cos(p\theta), \quad (38)$$

The variables i_a, U_a, i_b and U_b in the above equation represent the control currents supplied to the A and B phases, as well as the corresponding phase voltages. However, the variables R and L represent the resistance and inductance values of the motor phases, while K_m represents the motor torque constant, ω and and θ represent the angular speed and position of the motor, and p represents the number of rotor teeth of the stepper motor. The mechanical structure of the system establishes a direct relationship between the angular position (denoted as θ) of the motor and its linear position (denoted as d_i^T in

Equation (35)). The motor's output torque, which is influenced by the control current, can be mathematically represented as follows:

$$K_m\{-i_a sin(p\theta) + i_b cos(p\theta)\} - T_L = J\frac{d\omega}{dt}, +K_v\omega \quad (39)$$

In the above equation, J, K_v, and T_L indicate the motor shaft's inertia, the coefficient of viscous damping, and the torque exerted on the motor shaft by the load, respectively. By using the Park transformation on the voltage and torque equations stated in Equations (36)–(39), we obtained the voltage and torque expressions specified on the $d - q$ axis, as shown in Equation (40).

$$\begin{gathered} U_d = Ri_d + L\tfrac{d}{dt}i_d - Lp\omega i_q, \\ U_q = Ri_d + L\tfrac{d}{dt}i_q - Lp\omega i_d + K_m\omega, \\ T_{motor} = K_m i_q - J\tfrac{d\omega}{dt} - K_v\omega, \end{gathered} \quad (40)$$

By equating Equation (40), which represents the motor output torque expression, with the inverse dynamic equation of the mechanical system, Equation (41) is obtained. This provides the dynamic equation for the whole system.

$$M(q)\ddot{q} + C\big(q,\dot{q}\big)\dot{q} + G(q) = K_m i_q - J\ddot{q} - K_v\dot{q}, \quad (41)$$

Equation (41) can be restated as Equation (42) via the execution of mathematical procedures.

$$(M(q) - J)\ddot{q} + \big(C\big(q,\dot{q}\big) + K_v\big)\dot{q} + G(q) = K_m i_q, \quad (42)$$

Equation (42) can be simplified to Equation (43);

$$M(q)\ddot{q} + N\big(q,\dot{q}\big) = K_m i_q = \tau(t), \quad (43)$$

Here, $N\big(q,\dot{q}\big) = \big(C\big(q,\dot{q}\big) + K_v\big)\dot{q} + G(q)$.

3. Controller Design

3.1. PID Controller Design

A PID control equation is an equation that mathematically expresses the behavior of a proportional–integral–derivative controller [45]. The control equation is generally calculated as expressed in Equation (44). In Equation (44), $u(t)$ represents the control signal. The expression $e(t)$ is used as an error representation. The difference between the set point and the output of the actual process, that is, $r(t)$ is the reference desired value, $y(t)$ is the output of the system, and $e(t) = r(t) - y(t)$.

$$u(t) = k_i\int_0^t e(t)dt + k_p e(t) + k_d\frac{de(t)}{dt}, \quad (44)$$

The equation involves three coefficients: k_p, k_i, and k_d. The proportional coefficient, k_p, directly influences the output based on the error. The integral coefficient, k_i, determines the cumulative effect of the error over time. Lastly, the derivative coefficient, k_d, governs the impact of changes in the error on the output. The integral $\int_0^t e(t)dt$ represents the accumulation of mistakes over a period of time. This equation governs the output of the PID controller. To expedite the attainment of the desired set point and minimize error, this equation incorporates the immediate error value, its cumulative total, and its rate of change. The parameters k_p, k_i, and k_d are used to fine-tune the performance of the controller.

3.2. Sliding Mode Controller Design (SMC)

In the sliding mode control system, joint space trajectories are compelled to reach a sliding manifold within a finite time, known as the reachability phase. Subsequently, these trajectories are constrained to indefinitely remain on the manifold during the sliding phase [46]. The objective of the tracking control issue in the joint space is to precisely move the joint position $\boldsymbol{q}$ to the desired location $\boldsymbol{q_d}$. This difference between the $\boldsymbol{q}$ and $\boldsymbol{q_d}$ can be defined as the tracking error $\widetilde{\boldsymbol{q}}$.

$$\widetilde{\boldsymbol{q}} = \boldsymbol{q} - \boldsymbol{q_{d,}} \tag{45}$$

The sliding surface is determined using the following equation:

$$\boldsymbol{s} = \dot{\widetilde{\boldsymbol{q}}} - \boldsymbol{\lambda}\widetilde{\boldsymbol{q}}, \tag{46}$$

where $\lambda = diag[\lambda_1,\ \lambda_2, \ldots, \lambda_4]$ represents a diagonal positive definite matrix serving as a weighting parameter. The design of the controller can be expressed as the task of deriving a control law for the input vector τ that satisfies the individual sliding conditions of the following form:

$$\frac{1}{2}\frac{d}{dt}{s_i}^2 \leq -\eta_i|s_i| \qquad\qquad (\eta_i > 0), \tag{47}$$

Fulfilling Equation (47) results in the surface becoming an invariant set. Moreover, it suggests that disruptions or unpredictable changes may be accepted without affecting the stability of the surface as a fixed set. The optimal approximation $\hat{\boldsymbol{\tau}}$ of a control rule that would result in $\dot{s} = 0$ is as follows:

$$\hat{\boldsymbol{\tau}} = \hat{\boldsymbol{M}}\ddot{\boldsymbol{q}} + \hat{\boldsymbol{N}} - \boldsymbol{A}\boldsymbol{s}, \tag{48}$$

where $\hat{\boldsymbol{M}}$ and $\hat{\boldsymbol{N}}$ are estimates of $\boldsymbol{M}$ and $\boldsymbol{N}$, and $A = diag[a_1, \ldots a_4]$ is a diagonal positive definite constant matrix. To fulfill the sliding condition defined in Equation (47) in the presence of uncertainties in the dynamics, the term $\hat{\boldsymbol{\tau}}$ could be introduced to ensure discontinuity across the surface. Consequently, the control input becomes the following:

$$\boldsymbol{\tau} = \hat{\boldsymbol{\tau}} - \boldsymbol{F}sgn(\boldsymbol{s}), \tag{49}$$

Substituting Equation (49) into Equation (43) leads to the following:

$$\boldsymbol{M}\dot{\boldsymbol{s}} + (\boldsymbol{N} + \boldsymbol{A})\boldsymbol{s} = \Delta\boldsymbol{f} - \boldsymbol{Fsgn}(\boldsymbol{s}), \tag{50}$$

where $\Delta\boldsymbol{f}$ represents the estimation error, defined as $\Delta\boldsymbol{f} = \left(\hat{\boldsymbol{M}} - \boldsymbol{N}\right)\ddot{\boldsymbol{q}} + \left(\hat{\boldsymbol{N}} - \boldsymbol{N}\right)$, and it is assumed that the estimation error is bounded by a known quantity denoted as $\boldsymbol{F}$.

$$|\Delta f|_{bound} \leq F, \tag{51}$$

In order to demonstrate the convergence to the sliding mode, the variable $\boldsymbol{s}$ must approach zero within a specified duration. In order to achieve this objective, the Lyapunov approach may be used to derive a control rule that ensures the stability of the system. Choosing a Lyapunov function can be defined with the following equation:

$$\boldsymbol{V} = \frac{1}{2}\boldsymbol{s^T M s} \tag{52}$$

Since $\boldsymbol{M}$ is the symmetric and positive definite, then $\neq 0$ $\boldsymbol{V} > 0$. Additionally, differentiating Equation (52) and using Equation (50), the following equation is true:

$$\dot{\boldsymbol{V}} = \boldsymbol{s^T}[-(\boldsymbol{N} + \boldsymbol{A})\boldsymbol{s} + \Delta\boldsymbol{f} - \boldsymbol{F}sgn(\boldsymbol{s}) + \boldsymbol{Ns}] = \sum_{i=1}^{n} \boldsymbol{s_i}[\Delta\boldsymbol{f_i} - \boldsymbol{F_i}sgn(\boldsymbol{s_i})] - \boldsymbol{s^T A s} \leq 0 \tag{53}$$

Using Equation (51) for the $s_i > 0$ and $s_i < 0$ conditions, Equation (53) provides an exponentially stable system. In practical applications, the control rule described in Equation (49) may lead to rapid and repetitive oscillations known as chattering, particularly in situations involving high frequency switching. In order to decrease the control's chattering activity, the high-frequency switching function sgn may be approximated using a smooth-bounded saturation function sat.

Figure 6 illustrates the block diagram of the sliding mode control implementation for the manipulator, showcasing that the input is the desired trajectory of the manipulator involving both translation and orientation motions. The controller employs the inverse kinematic Equations (5) and (6) to transform the desired position and orientation of the manipulator into the necessary actuator angles. These angles are subsequently utilized as set-points for the six local controllers. The controller then executes the required control actions on the hybrid stepper motor drivers, enabling the accurate rotations of each input link and achieving the desired angles.

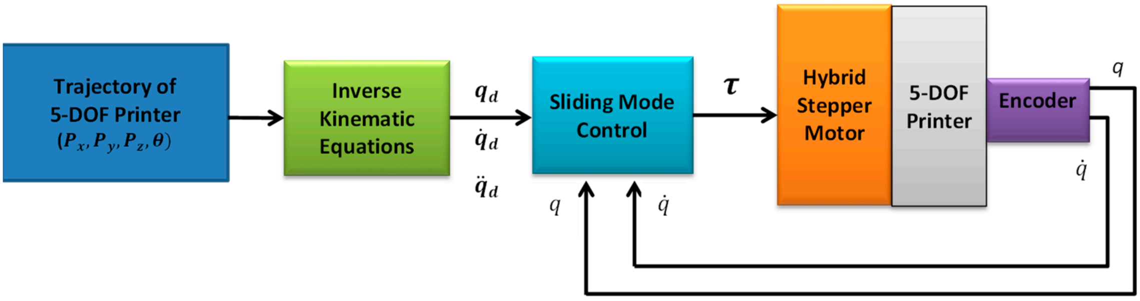

Figure 6. Block diagram of the sliding mode control process.

4. Experimental Results

The concept design of the 5-DOF robotic system with a parallel kinematic structure is shown in Figure 7. All values related to the limbs of the proposed system are presented in Table 1.

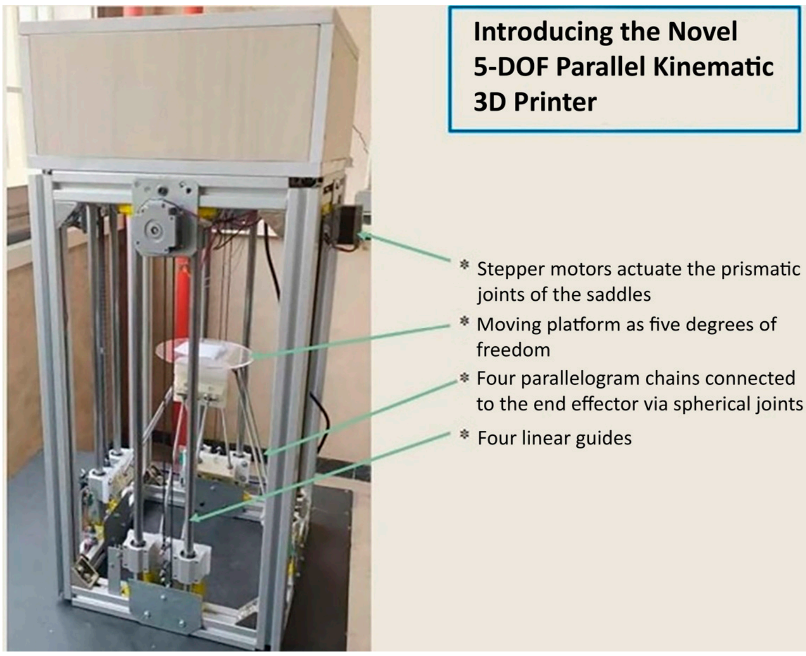

Figure 7. The proposed system with a completed design.

Table 1. Measurement values of all the mechanical subcomponents used in the system's design.

Parameters	Values
$l_{1,3,4}$	461 (mm)
l_2	561 (mm)
$c_{1,3}$	30 (mm)
$c_{2,4}$	0 (mm)
${}^{P}r_2$	[0; 196; 21] (mm)
${}^{P}r_4$	[0; 226; 21] (mm)
${}^{P}r_E$	[0; 99; −50.37] (mm)
${}^{P}r_P$	[0; 98.5; −222] (mm)
${}^{P}I_P$	$\begin{bmatrix} 4.5 & 0 & 0 \\ 0 & 2.6 & -0.01 \\ 0 & -0.01 & 2.6 \end{bmatrix} \times 10^{-2}(\text{kg}\cdot\text{m}^2)$
$m_{sad,1-4}$	0.64 (kg)
$m_{l,1,3,4}$	0.36 (kg)
$m_{l,2}$	0.43 (kg)
${}^{Li}I_{l,1,3,4}$	$\text{diag}(0.009; 6.5; 6.5) \times 10^{-2}\left(\text{kg}\cdot\text{m}^2\right)$
${}^{Li}I_{l,2}$	$\text{diag}(0.01; 11.5; 11.5) \times 10^{-2}\left(\text{kg}\cdot\text{m}^2\right)$
$m_{Con,1,3}$	0.25 (kg)
m_p	6.62 (kg)
${}^{P}b_1$	[−53; −98.5; −25] (mm)
${}^{P}b_2$	[0; 97.50; −4] (mm)
${}^{P}b_3$	[243; −91; −42] (mm)
${}^{P}b_4$	[29; 243; −42] (mm)

First of all, the operating performance of the designed system was evaluated. Translational and rotational motion experiments were conducted in the specified reference trajectory based on the established kinematic equation and control algorithm. The block diagram of the 5-DOF parallel 3D printer control system is shown in Figure 8. As can be seen in the figure, microprocessor coded STM32F405RB ARM Cortex M4 168 MHz (Texas Instrument, USA) and TMC262 stepper motor drivers were used in this study. The main task of the microprocessor was to produce the appropriate PWM signals needed by the stepper motor drivers according to the kinematics and controller equations. In addition, the microprocessor could simultaneously read the encoder information connected to the motors from the digital ports and use them as feedback information. The resolution per revolution of each encoder was 4096. The angular position accuracy was 0.002 degrees thanks to the 4x quadrature feature of the microprocessor. Two-phase Nema23 stepper motors (Oriental Motor USA Corp., Torrance, CA, USA) were used in the designed system. The coil resistance of these motors was 1.4 ohm, the inductance was 2.5 mH, the holding torque was 1.45 Nm, and the acceleration torque was 1.1 Nm.

Four distinct tests were conducted on the proposed system shown in Figure 7. The tests aimed to evaluate the system's mobility and compare the performance of the sliding mode controller with the standard PID controller. The performance of the four stepper motors in the planned system was evaluated based on the kinematic equation and control algorithms that were created. The tests assessed the translational and rotational capacities of the moveable table, which was coupled to the stepper motors, based on the specified reference. The control parameters used in all experiments for the controllers used in this study were $K_p = 5.135$, $K_i = 1.136$, $K_d = 0.022$, and $\lambda = 2.74$.

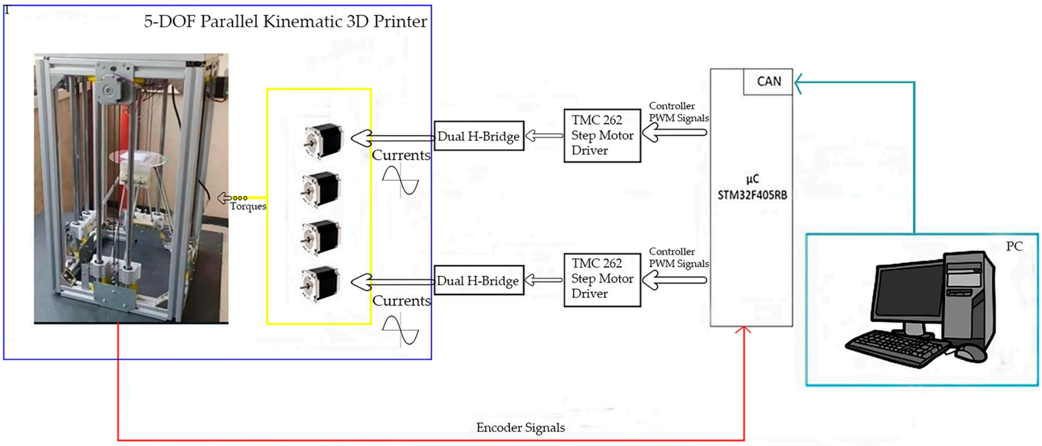

Figure 8. The controller block diagram of the proposed system.

4.1. Case One

First of all, we aimed for the moving table to move from the starting coordinates $x = 0$, $y = 0$, $z = 0$, and $\theta = 0^o$ to the reference coordinates $x = 0$, $y = 0$, $z = 15$ cm, and $\theta = 0^o$ in 1.5 s. In other words, the movable table was intended to move 15 cm upwards in the z coordinate without any orientation changes. In order for this reference to be realized by the system, according to the kinematic equations, the first and third motors must turn to the right at an angular position value of 12.54 radians, and the second and fourth motors must turn to the right in a similar manner at an angular position value of 19.32 radians. According to kinematic analysis, the reason why the first and third motors rotate less than the second and fourth motors is that the connection points of the second and fourth motors to the moving table are different compared to the first and third motors. According to the experimental results, the angular position changes of the motors are presented in Figure 9a,b. In all the drawn graphs, zoom images were included in order to clearly show the system settling time, steady-state error, and corresponding controller performance. When Figure 9a,b is examined, it is seen that if the motors in question are moved with sliding mode control instead of PID control, the table reaches the reference value faster. In other words, while the settling time of the motors was faster with the sliding mode controller, the steady-state error values were lower. In addition, in order to compare the performance of the proposed sliding mode controller with the classical PID controller, the root-mean-square error (MSE) and integral-square error (ISE) values of the system response occurring after the settling time were calculated, and these values are presented in Table 2. Since the sliding mode controller was based on the system model, a faster and more robust response was achieved. In addition, lower average error and integral error values were obtained in the SMC controller compared to the PID controller. The sliding mode controller produced better results than the traditional PID controller because it was based on the dynamic model of the system and was robust against disturbance effects during the motion.

Table 2. Outcomes of the case one applications.

Case 1	Settling Time (s)	MSE	ISE
Motor 1 SMC	0.512	6.94×10^{-4}	4.82×10^{-7}
Motor 3 SMC	0.511	6.49×10^{-4}	4.21×10^{-7}
Motor 1 PID	0.557	0.002	4.15×10^{-6}
Motor 3 PID	0.551	0.0022	4.94×10^{-6}
Motor 2 SMC	0.786	0.002	3.90×10^{-6}
Motor 4 SMC	0.778	0.002	3.97×10^{-6}
Motor 2 PID	0.818	0.0062	3.81×10^{-5}
Motor 4 PID	0.805	0.0056	3.09×10^{-5}

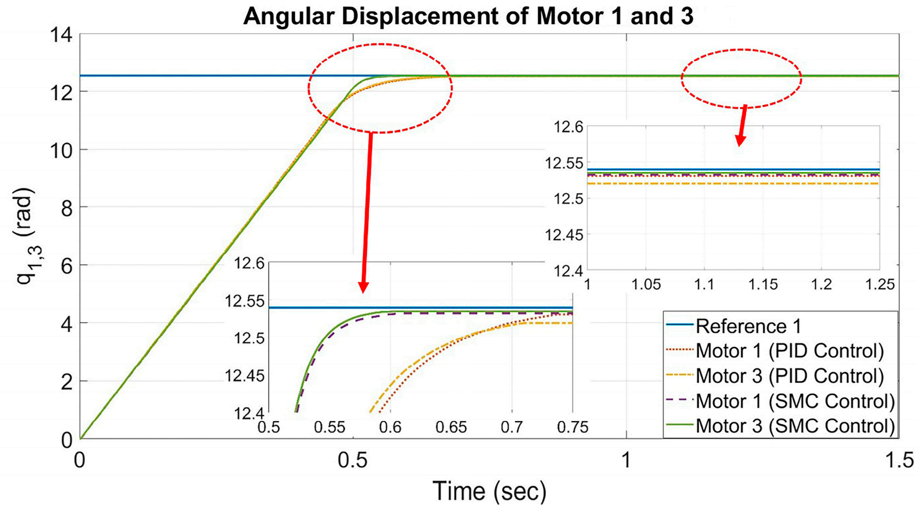

(**a**)

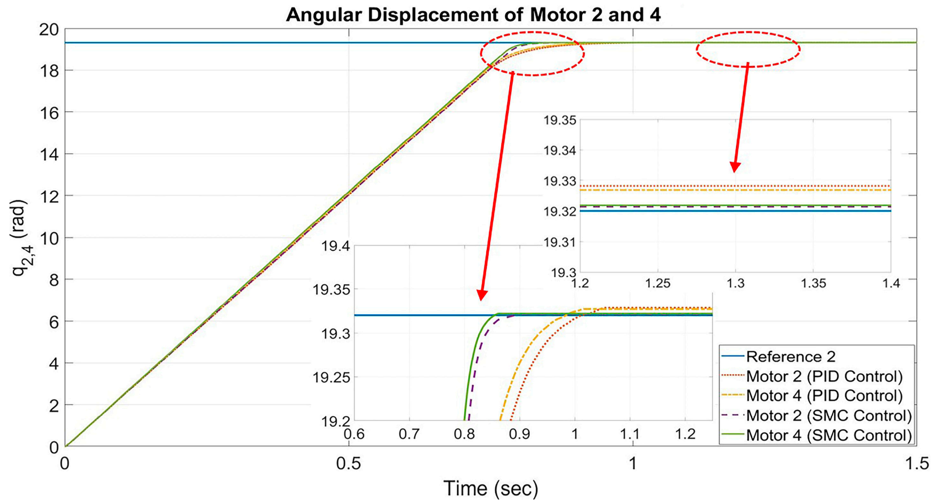

(**b**)

Figure 9. (**a**) Position change of the motors for case one and (**b**) position change of the motors for case one.

4.2. Case Two

As another reference value, the moving table moved from the starting coordinate of $x = 0$, $y = 0$, $z = 15$ cm, and $\theta = 0^o$ to the reference coordinate of $x = 15$ cm, $y = 0$, $z = 15$ cm, and $\theta = 0^o$ in 1.5 s. In other words, the movable table was intended to move 15 cm to the right only on the x-axis at a height of $z = 15$ cm without any orientation. In order for this reference to be realized by the system, according to the kinematic equations of the system, the first and third motors must turn leftward at an angular position value of -18.23 radians, and the second and fourth motors must turn rightward at an angular position value of 15.87 radians. According to the experimental results, the angular position changes of the motors are presented in Figure 10a,b. In this experiment, in order to compare the performance of the proposed sliding mode controller with the classical PID controller, the MSE and ISE values of the response occurring after the settling time were calculated, and these values are presented in Table 3. Although the torque values falling on the motor shafts are higher in this translational movement, a faster and more robust response was provided because the sliding mode controller is model based. As a result, lower average error values and integral error values were obtained in the SMC controller compared to the PID controller.

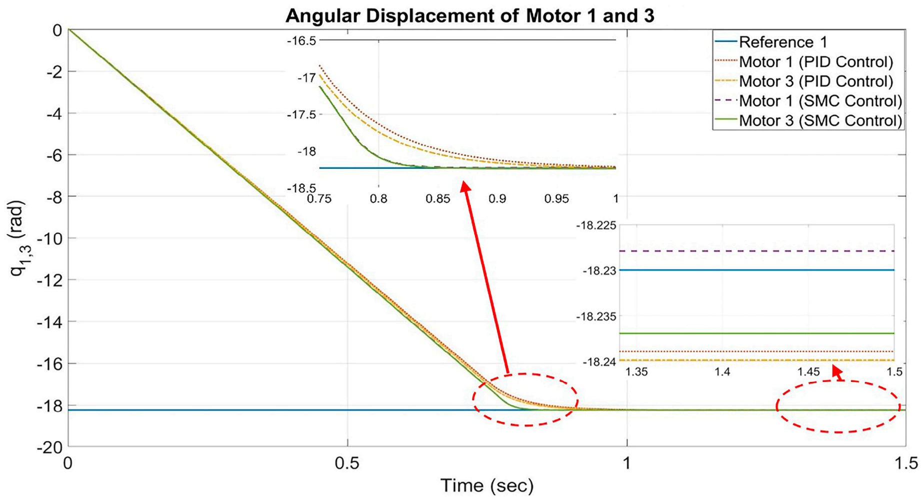

(a)

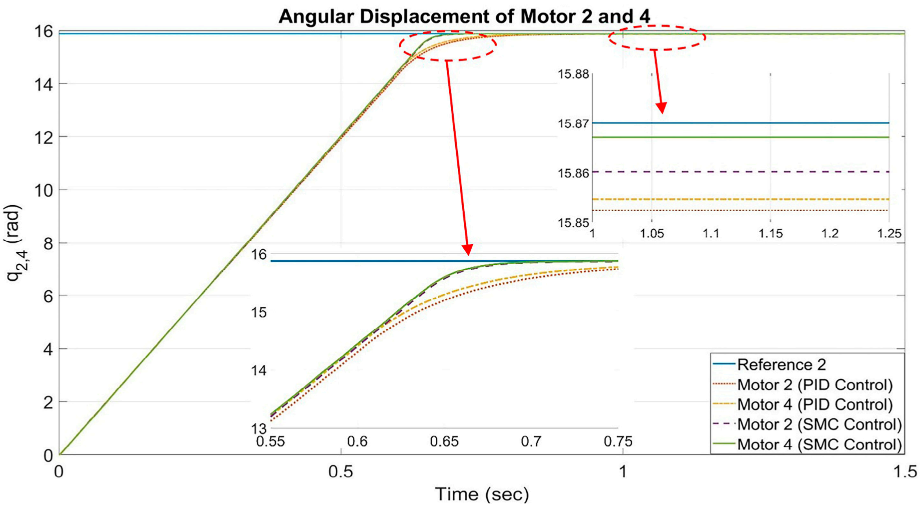

(b)

Figure 10. (**a**) Position change of the motors for case two. (**b**) Position change of the motors for case two.

Table 3. Outcomes of the case two applications.

Case 2	Settling Time (s)	MSE	ISE
Motor 1 SMC	0.784	0.0017	2.92×10^{-6}
Motor 3 SMC	0.783	0.0018	3.24×10^{-6}
Motor 1 PID	0.829	0.0057	3.25×10^{-5}
Motor 3 PID	0.816	0.0049	2.45×10^{-5}
Motor 2 SMC	0.65	0.0012	1.46×10^{-6}
Motor 4 SMC	0.648	0.0011	1.26×10^{-6}
Motor 2 PID	0.697	0.0044	1.93×10^{-5}
Motor 4 PID	0.683	0.0038	1.46×10^{-5}

4.3. Case Three

In the third experimental study, we aimed for the moving table to move from the starting coordinates $x = 0$, $y = 0$, $z = 15$, and $\theta = 0^o$ to the reference coordinates $x = 0$, $y = 15$ cm, $z = 15$ cm, and $\theta = 0^o$ in 1.5 s. In other words, the movable table was intended to move 15 cm to the right only on the y-axis at a height of $z = 15$ cm without any orientation. In order for this reference to be realized by the system, according to the kinematic equations, the first and third motors must turn to the right at an angular position of 11.45 radians, and the second and fourth motors must turn to the right at an angular position of 23.11 radians. According to the experimental results, the angular position changes of the motors are presented in Figure 11a,b. A similar situation was obtained in this experiment, and the obtained values are presented in Table 4. In particular, the MSE and ISE values were lower in the sliding mode controller, and the targeted reference values were reached in a shorter time, resulting in lower settling times.

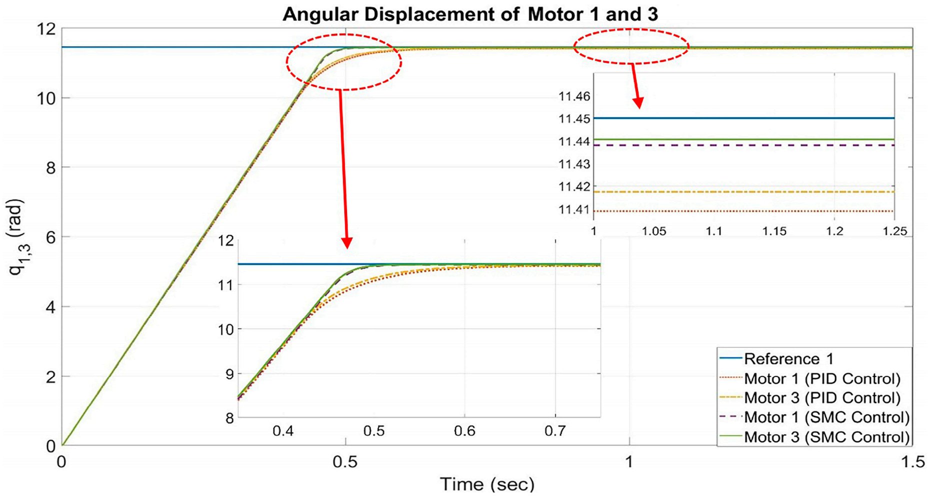

(**a**)

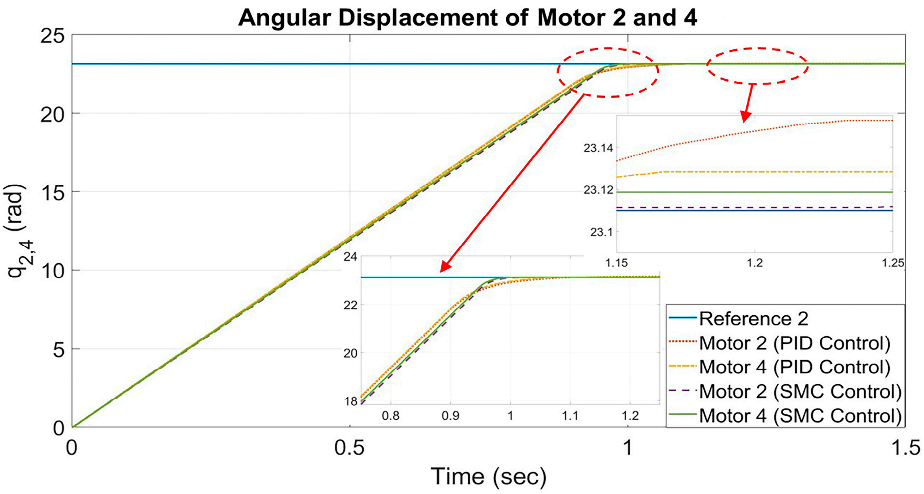

(**b**)

Figure 11. (**a**) Position change of the motors for case three. (**b**) Position change of the motors for case three.

Table 4. Outcomes of the case three applications.

Case 3	Settling Time (s)	MSE	ISE
Motor 1 SMC	0.471	6.30×10^{-4}	3.96×10^{-7}
Motor 3 SMC	0.468	5.59×10^{-4}	3.13×10^{-7}
Motor 1 PID	0.532	0.0034	1.16×10^{-5}
Motor 3 PID	0.518	0.0026	6.87×10^{-6}
Motor 2 SMC	0.95	0.0039	1.49×10^{-5}
Motor 4 SMC	0.946	0.0035	1.20×10^{-5}
Motor 2 PID	0.959	0.0114	1.29×10^{-4}
Motor 4 PID	0.951	0.0095	9.07×10^{-5}

4.4. Case Four

Finally, we aimed for the moving table to orient itself from the initial coordinates $x = 0, y = 0, z = 15$, and $\theta = 0^o$ to the final coordinates $x = 0$, $y = 0$, $z = 15$ cm, and $\theta = 10^o$ in 1.5 s. In other words, the movable table was intended to rotate only 10 degrees to the right around the x-axis without any translational movement. In order for this reference to be realized by the system, according to the kinematic equations of the system, the first and third motors must turn leftward at an angular position value of -7.21 radians, and the second and fourth motors must turn rightward at an angular position value of 19.15 radians. According to the experimental results, the angular position changes of the motors are presented in Figure 12a,b. It is inevitable that different torque values affect the motors in the orientation movement, which is one of the most important features of the desired movement. When Figure 12a,b and Table 5 are examined, the performance of the sliding mode controller is quite better than that of the classical PID controller. Although higher torque values affected the motor shafts, the sliding mode controller was not affected by this situation and successfully performed these difficult reference trajectories faster and with lower error values.

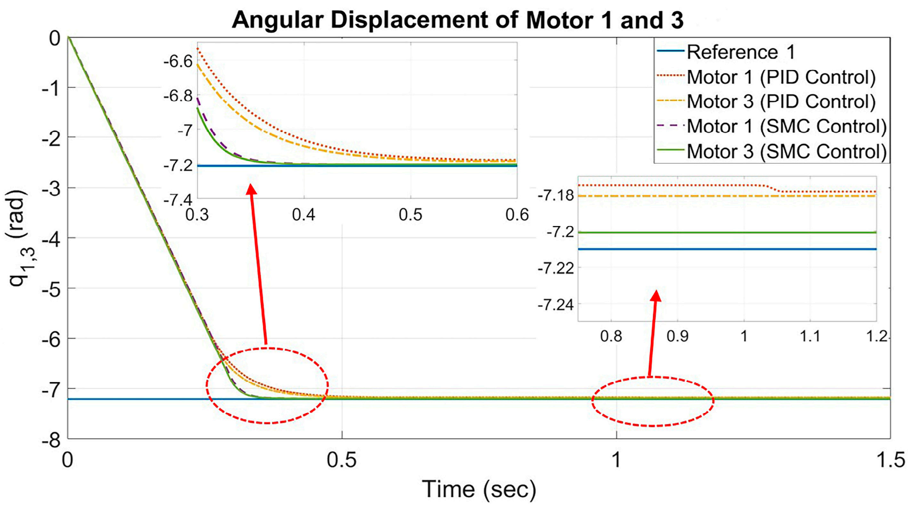

(**a**)

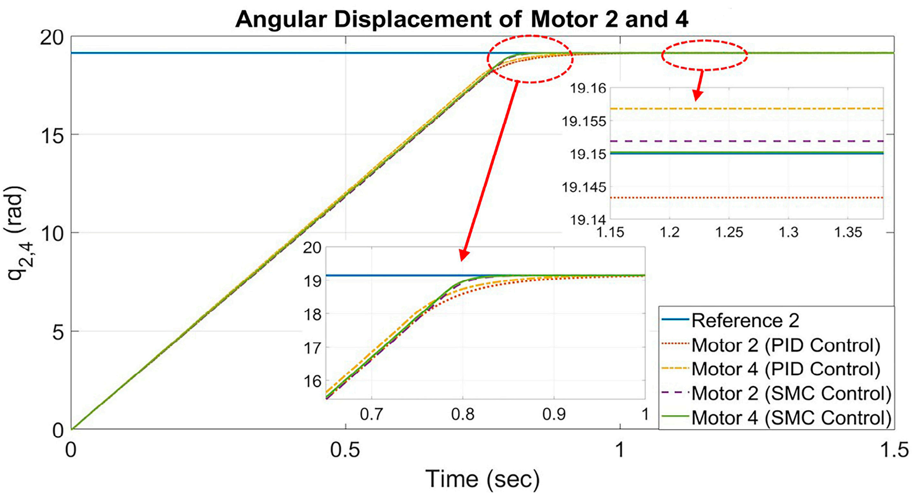

(**b**)

Figure 12. (**a**) Position change of the motors for case four. (**b**) Position change of the motors for case four.

Table 5. Outcomes of the case four applications.

Case 4	Settling Time (s)	MSE	ISE
Motor 1 SMC	0.321	2.72×10^{-4}	7.39×10^{-8}
Motor 3 SMC	0.317	2.65×10^{-4}	7.04×10^{-8}
Motor 1 PID	0.402	0.0018	3.08×10^{-6}
Motor 3 PID	0.384	0.0014	2.03×10^{-6}
Motor 2 SMC	0.791	0.0019	3.52×10^{-6}
Motor 4 SMC	0.787	0.0019	3.78×10^{-6}
Motor 2 PID	0.823	0.0065	4.22×10^{-5}
Motor 4 PID	0.805	0.0054	2.91×10^{-5}

4.5. Case Five: Experimental Outcomes of Producing a Real Part

In this part of the experimental study, real parts were produced using the designed system and the results are shared herein. By using printers with degrees of freedom of more than three axes, limitations, such as the need for support in the manufacture of complex parts, are eliminated, and the print time is reduced due to the use of a 5-DOF parallel mechanism. In addition, due to the possibility of defining the print directions of the parts, increasing the strength of the final part can be achieved. By using a five-axis 3D printer, the parts that normally require support with angles greater than 45 degrees can be printed without the need for a support system and do not use a support system at all. It is expected that due to the lack of support, a significant improvement is achieved in the surface quality of the final product, and the strength of the final piece increases due to the ability to print in different directions. The speed and quality of printing also increase, and the cost of printing decreases.

According to the advantages of the five-axis printer compared to the three-axis printer, it is necessary to print a part using the three-axis printer. Therefore, to print the part using both printers, it is necessary to check the output parameters and examine the advantages and disadvantages of both printers. According to the conducted studies, it is expected that the surface quality of the part produced using a five-axis printer is better than that of a three-axis printer. Among the reasons for the superiority of the surface quality in five-axis printing, parts that need support for manufacturing can be printed without support. In five-axis printing, the direction of the nozzle can always be set perpendicular to the surface, which is known as tangential printing. In the following, the same part is produced with two different printers, and different parameters in the part produced by each printer are compared with each other. The selected piece for this research was an elbow-shaped pipe. This piece was produced once by a three-axis printer (Figure 13a,b) and another time using a five-axis printer (Figure 14a,b). In each of the devices, parameters such as print time, surface quality, appearance of the part, etc., were checked and compared with each other.

According to the examination of the parts produced by both methods and due to the layer-by-layer method of creating a 3D printer, the surface on which the nozzle is perpendicular during printing has better mechanical properties than the other directions. On this basis, the part produced with a five-axis printer is stronger than the three-axis mode.

Also, due to the fact that during the removal of the support, the surface of the piece is damaged and becomes rougher, parts printed with a 3D printer have a lower level of quality. In addition, when printing perpendicular to the surface in the five-axis printing, a smoother surface texture is observed on the surface of the parts produced using this method. The production speed for the part shown in Figure 14, with the five-axis method being approximately three times that of the part produced in Figure 13 with the three-axis method.

Regarding the temperature of the printing parts, considering that the material selected for printing was PLA, the standard temperature range for printing is approximately 190 to 220 degrees Celsius. In this research, the printing temperature was 200 degrees Celsius. Additionally, Simplify 3D software, which was used to produce the G-codes of this part, adjusted the temperature of the layers of the different parts by adjusting the print speeds at different stages, and hence, there were no special complications or distortions of the surfaces of the parts due to the lack of adjustment of the print temperature.

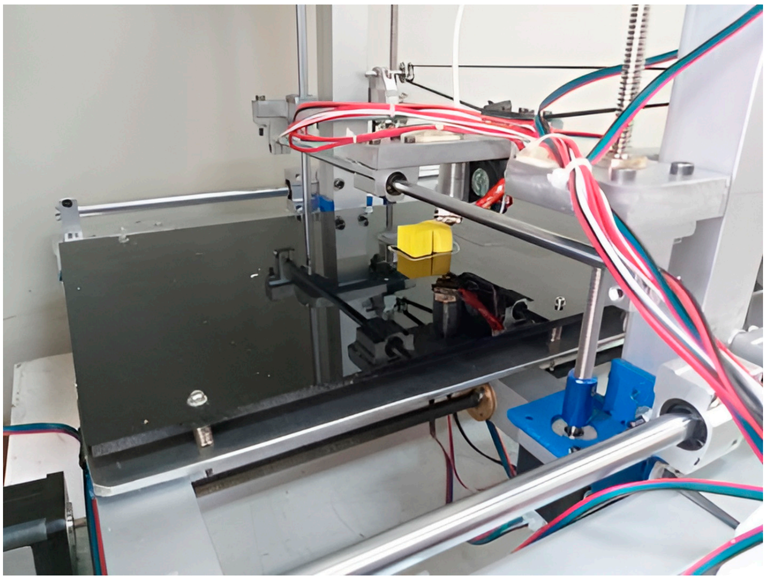

(**a**)

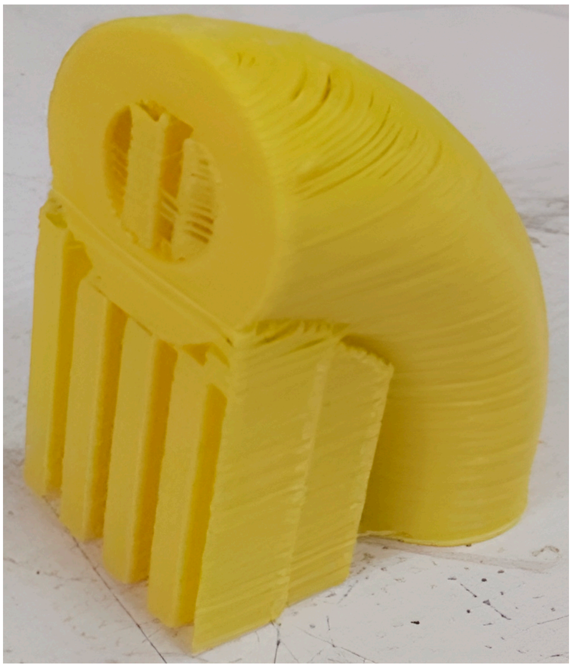

(**b**)

Figure 13. (**a**) The part printed in a three-axis printer with a support structure. (**b**) The printed piece has a support structure.

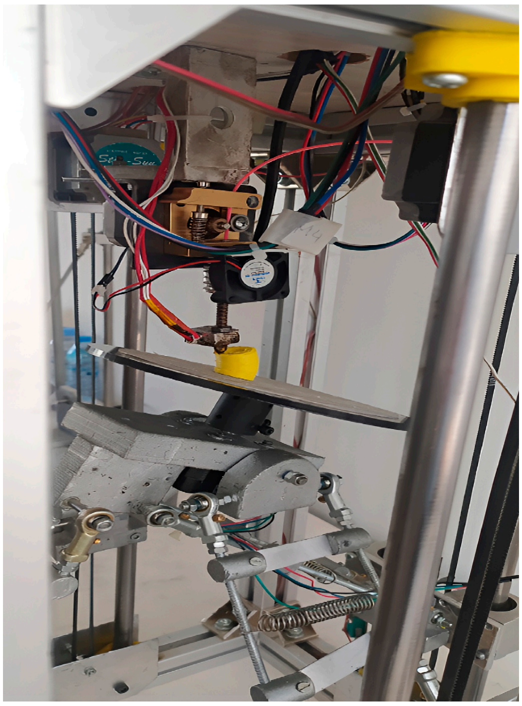

(a)

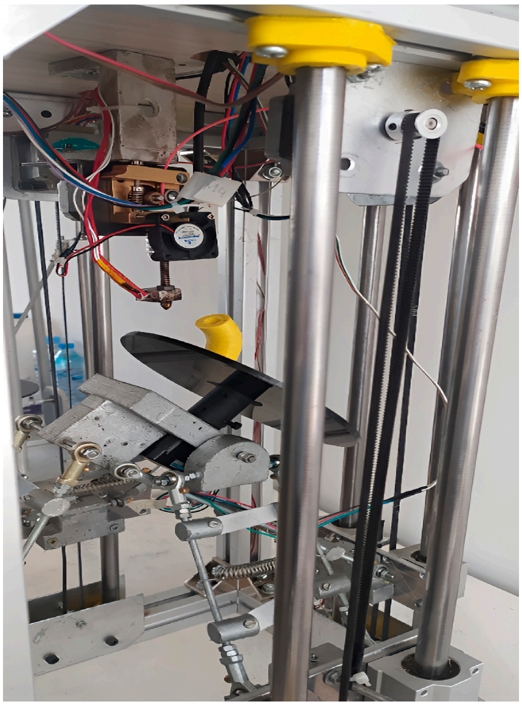

(b)

Figure 14. (**a**) The piece printed in a 5-axis printer. (**b**) The part printed in a five-axis printer without a support structure.

5. Discussion

The research introduces a novel robotic system with a parallel kinematic framework, including five degrees of freedom. This system represents a significant advancement in additive manufacturing technology. The system is notable for its parallel kinematic structure, which allows for increased precision and the possibility of better operating speed. Furthermore, the ability to rotate along the x and z-axes facilitated the creation of intricate product geometries, hence expanding the range of potential applications in numerous industries. The potential benefits of this design for the industry include enhanced product quality, expedited production processes, and the simplified manufacturing of intricate components. Moreover, an increased number of degrees of freedom provides designers and engineers with a greater level of adaptability in the manufacturing environment. Nevertheless, more investigation and analysis are required to facilitate the commercialization of this innovative design and assess its feasibility on a large-scale industrial level. For instance, the inclusion of the nozzle architecture in 3D printers is necessary for the system, and it is vital to conduct performance evaluations of the system. Ongoing work is being conducted on the system, and further studies are scheduled to assess the production performance of the system. Furthermore, its purpose is to assess the system's control performance in relation to newly established control strategies. Furthermore, the investigation will assess the appropriateness of the design for various sectors of the industry and its superiority compared to alternative manufacturing techniques.

In future work, material production tests will be carried out by adding a nozzle and a drilling component to the designed system. In addition, fractional order PID and adaptive sliding mode control methods will be developed to further strengthen the control performance of the system.

Author Contributions: Conceptualization, A.D., K.K.A. and M.M.; methodology, A.D., K.K.A. and M.M.; software, A.D. and K.K.A.; validation, A.D., K.K.A. and S.G.; formal analysis, A.D. and K.K.A.; investigation, A.D. and K.K.A.; resources, M.M. and S.A.; data curation, A.D. and G.K.; writing—original draft preparation, A.D. and K.K.A.; writing—review and editing, K.K.A. and A.D.; visualization, S.A. and A.D.; supervision, A.D.; project administration, A.D. and K.K.A.; funding acquisition, A.D. All authors have read and agreed to the published version of the manuscript.

Funding: This paper is based upon work supported by the TUBITAK authority under project number 119N707.

Data Availability Statement: The data presented in this study are available on request from the corresponding author.

Conflicts of Interest: The authors declare no conflicts of interest.

References

1. Li, L.; Haghighi, A.; Yang, Y. A Novel 6-Axis Hybrid Additive-Subtractive Manufacturing Process: Design and Case Studies. *J. Manuf. Process.* **2018**, *33*, 150–160. [CrossRef]
2. The Economist. A Third Industrial Revolution: As Manufacturing Goes Digital, It Will Change Out of All Recognition, Says Paul Markillie. And Some of the Business of Making Things Will Return to Rich Countries. *The Economist*, 21 April 2012.
3. Sun, Y.; Liu, Y.; Pancheri, F.; Lueth, T.C. LARG: A Lightweight Robotic Gripper With 3-D Topology Optimized Adaptive Fingers. *IEEE/ASME Trans. Mechatron.* **2022**, *27*, 2026–2034. [CrossRef]
4. Bendowska, K.; Zawadzki, P. Development and Verification of a Simulation Model of an Automated Assembly Line. *Appl. Sci.* **2023**, *13*, 10142. [CrossRef]
5. Barari, A.; Tsuzuki, M.S.G. Smart Manufacturing and Industry 4.0. *Appl. Sci.* **2023**, *13*, 1545. [CrossRef]
6. Najafabadi, R.H.; Goto, T.G.; Falheiro, M.S.; Martins, C.T.; Barari, A.; Tsuzuki, M.S.G. Smart Topology Optimization Using Adaptive Neighborhood Simulated Annealing. *Appl. Sci.* **2021**, *11*, 5257. [CrossRef]
7. Urhal, P.; Weightman, A.; Diver, C.; Bartolo, P. Robot Assisted Additive Manufacturing: A Review. *Robot. Comput.-Integr. Manuf.* **2019**, *59*, 335–345. [CrossRef]
8. Lu, Y.; Hu, B. Analyzing Kinematics and Solving Active/Constrained Forces of a 3SPU+UPR Parallel Manipulator. *Mech. Mach. Theory* **2007**, *42*, 1298–1313. [CrossRef]
9. Singh, Y.; Vinoth, V.; Kiran, Y.R.; Mohanta, J.K.; Mohan, S. Inverse Dynamics and Control of a 3-DOF Planar Parallel (U-Shaped 3-PPR) Manipulator. *Robot. Comput.-Integr. Manuf.* **2015**, *34*, 164–179. [CrossRef]
10. Pierrot, F.; Nabat, V.; Company, O.; Krut, S.; Poignet, P. Optimal Design of a 4-DOF Parallel Manipulator: From Academia to Industry. *IEEE Trans. Robot.* **2009**, *25*, 213–224. [CrossRef]
11. Liu, S.; Huang, T.; Mei, J.; Zhao, X.; Wang, P.; Chetwynd, D.G. Optimal Design of a 4-DOF SCARA Type Parallel Robot Using Dynamic Performance Indices and Angular Constraints. *J. Mech. Robot.* **2012**, *4*, 031005. [CrossRef]
12. Dong, G.; Sun, T.; Song, Y.; Gao, H.; Lian, B. Mobility Analysis and Kinematic Synthesis of a Novel 4-DOF Parallel Manipulator. *Robotica* **2016**, *34*, 1010–1025. [CrossRef]

13. de Almeida, P.L., Jr.; Lima, L.M.A.; de Almeida, L.F. A 3D-Printed Robotic System for Fully Automated Multiparameter Analysis of Drinkable Water Samples. *Anal. Chim. Acta* **2021**, *1169*, 338491. [CrossRef] [PubMed]
14. Pierrot, F.; Company, O. H4: A New Family of 4-DOF Parallel Robots. In Proceedings of the 1999 IEEE/ASME International Conference on Advanced Intelligent Mechatronics (Cat. No.99TH8399), Atlanta, GA, USA, 19–23 September 1999; pp. 508–513.
15. Choi, H.B.; Company, O.; Pierrot, F.; Konno, A.; Shibukawa, T.; Uchiyama, M. Design and Control of a Novel 4-DOFs Parallel Robot H4. In Proceedings of the 2003 IEEE International Conference on Robotics and Automation (Cat. No.03CH37422), Taipei, Taiwan, 14–19 September 2003; Volume 1, pp. 1185–1190.
16. Rolland, L.H. *The Manta and the Kanuk: Novel 4-DOF Parallel Mechanisms for Industrial Handling*; American Society of Mechanical Engineers Digital Collection: New York, NY, USA, 2021; pp. 831–844.
17. Briot, S.; Arakelian, V.; Guégan, S. Design and Prototyping of a Partially Decoupled 4-DOF 3T1R Parallel Manipulator With High-Load Carrying Capacity. *J. Mech. Des.* **2008**, *130*, 122303. [CrossRef]
18. Lu, Y.; Shi, Y.; Huang, Z.; Yu, J.; Li, S.; Tian, X. Kinematics/Statics of a 4-DOF over-Constrained Parallel Manipulator with 3 Legs. *Mech. Mach. Theory* **2009**, *44*, 1497–1506. [CrossRef]
19. Briot, S.; Bonev, I.A. Pantopteron-4: A New 3T1R Decoupled Parallel Manipulator for Pick-and-Place Applications. *Mech. Mach. Theory* **2010**, *45*, 707–721. [CrossRef]
20. Gogu, G. Structural Synthesis of Fully-Isotropic Parallel Robots with Schönflies Motions via Theory of Linear Transformations and Evolutionary Morphology. *Eur. J. Mech.-A/Solids* **2007**, *26*, 242–269. [CrossRef]
21. Yang, S.; Sun, T.; Huang, T. Type Synthesis of Parallel Mechanisms Having 3T1R Motion with Variable Rotational Axis. *Mech. Mach. Theory* **2017**, *109*, 220–230. [CrossRef]
22. Ye, W.; Fang, Y.; Guo, S. Design and Analysis of a Reconfigurable Parallel Mechanism for Multidirectional Additive Manufacturing. *Mech. Mach. Theory* **2017**, *112*, 307–326. [CrossRef]
23. Mahboubkhah, M.; Barari, A. Design and Development of a Novel 4-DOF Parallel Kinematic Coordinate Measuring Machine (CMM). *Int. J. Comput. Integr. Manuf.* **2019**, *32*, 750–760. [CrossRef]
24. Xie, F.; Liu, X.-J. Analysis of the Kinematic Characteristics of a High-Speed Parallel Robot with Schönflies Motion: Mobility, Kinematics, and Singularity. *Front. Mech. Eng.* **2016**, *11*, 135–143. [CrossRef]
25. Krut, S.; Company, O.; Nabat, V.; Pierrot, F. Heli4: A Parallel Robot for Scara Motions with a Very Compact Traveling Plate and a Symmetrical Design. In Proceedings of the 2006 IEEE/RSJ International Conference on Intelligent Robots and Systems, Beijing, China, 9–15 October 2006; pp. 1656–1661.
26. Krut, s.; Pierrot, F. Modelling of a 4 Axis Parallel Machine for Heavy Parts Handling. In *Parallel Kinematics Seminar*; Verlag Scripten: Freiburg im Breisgau, German, 2002; Volume 16, pp. 151–168.
27. Nabat, V.; Rodriguez, M.D.L.O.; Krut, S.; Pierrot, F. Par4: Very High Speed Parallel Robot for Pick-and-Place. In Proceedings of the 2005 IEEE/RSJ International Conference on Intelligent Robots and Systems, Edmonton, AB, Canada, 2–6 August 2005; pp. 553–558.
28. Zhang, J.; Liou, F. Adaptive Slicing for a Multi-Axis Laser Aided Manufacturing Process. *J. Mech. Des.* **2004**, *126*, 254–261. [CrossRef]
29. Clavel, R. Unmanned Robotic Delta Weapon Platform. Patent No CA2732697A1. WIPO Patent February 2011.
30. Pakzad, S.; Akhbari, S.; Mahboubkhah, M. Kinematic and Dynamic Analyses of a Novel 4-DOF Parallel Mechanism. *J. Braz. Soc. Mech. Sci. Eng.* **2019**, *41*, 561. [CrossRef]
31. Denavit, J.; Hartenberg, R.S. A Kinematic Notation for Lower-Pair Mechanisms Based on Matrices. *J. Appl. Mech.* **2021**, *22*, 215–221. [CrossRef]
32. Chace, M.A. Vector Analysis of Linkages. *J. Eng. Ind.* **1963**, *85*, 289–297. [CrossRef]
33. Duffy, J.; Rooney, J. A Foundation for a Unified Theory of Analysis of Spatial Mechanisms. *J. Eng. Ind.* **1975**, *97*, 1159–1164. [CrossRef]
34. Nanua, P.; Waldron, K.J. Direct Kinematic Solution of a Stewart Platform. In *1989 IEEE International Conference on Robotics and Automation*; IEEE Computer Society: Piscataway, NJ, USA, 1989; pp. 431–437.
35. Su, Y.X.; Zheng, C.; Duan, B.Y. Singularity Analysis of a 6 DOF Stewart Platform Using Genetic Algorithm. In Proceedings of the IEEE International Conference on Systems, Man and Cybernetics, Yasmine Hammamet, Tunisia, 6–9 October 2002; Volume 7, p. 6.
36. Wang, Z.; He, J.; Gu, H. Forward Kinematics Analysis of a Six-Degree-of-Freedom Stewart Platform Based on Independent Component Analysis and Nelder–Mead Algorithm. *IEEE Trans. Syst. Man Cybern. Part A* **2011**, *41*, 589–597. [CrossRef]
37. Dasgupta, B.; Mruthyunjaya, T.S. A Newton-Euler Formulation for the Inverse Dynamics of the Stewart Platform Manipulator. *Mech. Mach. Theory* **1998**, *33*, 1135–1152. [CrossRef]
38. Dasgupta, B.; Mruthyunjaya, T.S. Closed-Form Dynamic Equations of the General Stewart Platform through the Newton–Euler Approach. *Mech. Mach. Theory* **1998**, *33*, 993–1012. [CrossRef]
39. Craig, J.J. *Introduction to Robotics*; Pearson Educación: London, UK, 2006; ISBN 978-970-26-0772-4.
40. Spong, M.W.; Vidyasagar, M. *Robot Dynamics and Control*; John Wiley & Sons: Hoboken, NJ, USA, 2008.
41. Jazar, R.N. *Theory of Applied Robotics: Kinematics, Dynamics, and Control*; Springer International Publishing: Cham, Switzerland, 2022; ISBN 978-3-030-93219-0.
42. Matsui, N.; Nakamura, M.; Kosaka, T. Instantaneous Torque Analysis of Hybrid Stepping Motor. *IEEE Trans. Ind. Appl.* **1996**, *32*, 1176–1182. [CrossRef]

43. Bellini, A.; Concari, C.; Franceschini, G.; Toscani, A. Mixed-Mode PWM for High-Performance Stepping Motors. *IEEE Trans. Ind. Electron.* **2008**, *54*, 3167–3177. [CrossRef]
44. Baluta, G.; Coteata, M. Precision Microstepping System for Bipolar Stepper Motor Control. In Proceedings of the 2007 International Aegean Conference on Electrical Machines and Power Electronics, Bodrum, Turkey, 10–12 September 2007; pp. 291–296.
45. Franklin, G.F.; Powell, J.D.; Emami-Naeini, A. *Feedback Control of Dynamic Systems*; Pearson: London, UK, 2015; Volume 33.
46. Islam, S.; Liu, X.P. Robust Sliding Mode Control for Robot Manipulators. *IEEE Trans. Ind. Electron.* **2010**, *58*, 2444–2453. [CrossRef]